

Deterministic domain selection of antiferromagnets via magnetic fields

Sophie F. Weber¹ and Veronika Sunko²

¹Department of Physics, Chalmers University of Technology, SE-412 96 Gothenburg, Sweden

²Institute of Science and Technology Austria (ISTA), 3400 Klosterneuburg, Austria

(Dated: January 13, 2026)

Antiferromagnets (AFMs) hold promise for applications in digital logic. However, switching AFM domains is challenging, as magnetic fields do not couple to the bulk antiferromagnetic order parameter. Here we show that magnetic-field-driven switching of AFM domains can in many cases be enabled by a generic reduction of magnetic exchange at surfaces. We use statistical mechanics and Monte Carlo simulations to demonstrate that an inequivalence in magnetic exchange between top and bottom surface moments, combined with the enhanced magnetic susceptibility of surface spins, can enable deterministic selection of antiferromagnetic domains depending on the magnetic-field ramping direction. We further show that this mechanism provides a natural interpretation for experimental observations of hysteresis in magneto-optical response of the van der Waals AFM MnBi_2Te_4 . Our findings highlight the critical role of surface spins in responses of antiferromagnets to magnetic fields. Furthermore, our results suggest that antiferromagnetic domain selection via purely magnetic means may be a more common and experimentally accessible phenomenon than previously assumed.

Antiferromagnets (AFMs) have attracted recent interest because their staggered magnetization, or Néel vector, is a bit-like quantity suitable for logic and storage applications. Compared to ferromagnets (FMs), AFMs offer advantages such as robustness against stray magnetic fields and ultrafast magnetization dynamics [1, 2].

While the insensitivity of AFMs to moderate magnetic fields is beneficial for stability, it is traditionally thought to hinder both switching of the order parameter and deterministic control of the Néel vector. For fields weak compared to the AFM Heisenberg coupling J^{AFM} , the two AFM domains are degenerate (Fig. 1(a)). Stronger fields drive spin-flop (Fig. 1(b)) and spin-flip (Fig. 1(c)) transitions respectively, altering AFM order rather than enabling domain selection. As a result, domain control is often achieved through electric-field-based mechanisms, such as spin-orbit torques and magnetoelectric annealing, whose applicability relies on material-specific symmetries [3–6].

On the other hand, deterministic selection of AFM do-

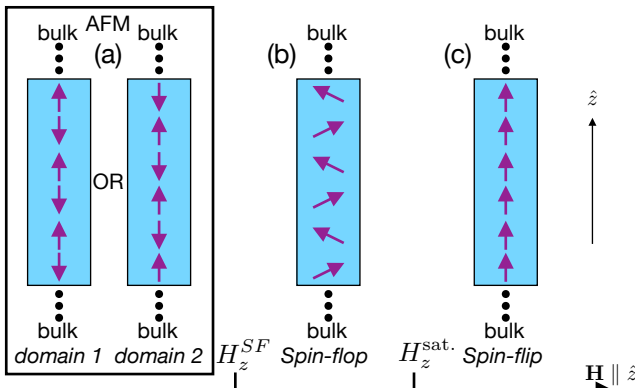


FIG. 1: Field response of a periodic bulk A-type AFM as a function of magnetic field strength H_z applied parallel to the easy axis. H_z^{SF} and $H_z^{\text{sat.}}$ denote the spin flop and the saturation field, respectively.

mains by a magnetic field has been reported in the layered antiferromagnet MnBi_2Te_4 (MBT) [7–11]. Spins in MBT are perpendicular to the layers, and assume the A-type AFM structure: spins in each layer are parallel to each other, and anti-parallel to those in neighboring layers. The field-evolution of MBT’s magnetic structure is therefore captured by Fig. 1, with arrows representing layer magnetization, implying that domain selection by a magnetic field should be impossible. Nonetheless, magnetic field-based control has been utilized to uncover unusual electrodynamic properties of the AFM state in MBT, including a magneto-optical Kerr effect (MOKE) whose sign is determined by the Néel vector [7–11]. Here we resolve this apparent contradiction by considering a key feature of real materials; surfaces, which are known to exhibit magnetic behavior distinct from the corresponding bulk [12–14].

In this Letter, we show using statistical mechanics and Monte Carlo (MC) simulations that the reduced effective Heisenberg exchange at AFM surfaces can drive the magnetic field response of the entire slab. In particular, if the AFM exchange on top and bottom surfaces is sufficiently different, ramping $|H_z|$ from above $|H_z^{\text{SF}}|$ to $H_z = 0$ leads to *deterministic* selection of a single AFM domain, with the Néel vector sign dependent on the direction of ramping. We use our MC results to model the MOKE signal as a function of magnetic field for thick flakes of MBT, and find very good agreement with recent experiments [11].

Although MBT inspired this work, the results are general for A-type AFMs. Given that inequivalence between opposite crystal surfaces is ubiquitous (for example, via growth on a substrate, interfacing with another material, or defects), magnetic field-based AFM domain selection is likely to be realized in many experimental systems.

Statistical Mechanics considerations— As a minimal model we consider a layered AFM with one spin per layer in the unit cell (we assume uniform intralayer FM cou-

pling), interlayer Heisenberg exchange J^{AFM} , and uniaxial single-ion anisotropy K along \hat{z} . The Hamiltonian for this system under an out-of-plane applied magnetic field H_z is given by

$$E = E_0 + J^{\text{AFM}} \sum_{ij} \hat{e}_i \cdot \hat{e}_j - K \sum_i (\hat{e}_i \cdot \hat{z})^2 - C \sum_i (S_i)^z H_z. \quad (1)$$

Here, the sum is over magnetic atoms in the unit cell; \hat{e}_i is the unit vector parallel to the magnetic moment on site i ; S_i is the magnetic moment of site i in μ_B , and C converts $\mu_B \cdot \text{T}$ to eV. For the following arguments, we start with H_z along the $+\hat{z}$ at a strength above the spin-flop field H_z^{SF} , with spins canted along $+\hat{z}$ (Fig. 2(a)). We then consider how the presence of vacuum-terminated top and bottom surfaces can alter the evolution to collinear AFM domain states around $H_z = 0$ as $+H_z \rightarrow 0 \rightarrow -H_z$ (a “ramp-down” procedure).

In a bulk AFM each layer has two neighboring layers, yielding an effective exchange $J^{\text{tot}} = 2J^{\text{AFM}}$. In contrast, surface spins have one neighboring layer, and a *halved* total exchange compared to interior spins. As a result, the AFM coupling of surface spins overcomes the Zeeman energy at a lower field than of interior spins, stabilizing a field window below H_z^{SF} where both surface spins align with H_z . This enforces a multidomain AFM state. In our toy model the domain wall corresponds to a ferromagnetically aligned bilayer (BL); in the center panel of Figs. 2(a,b) we illustrate its three possible positions for an $N = 6$ slab, and label the corresponding configurations BL1, BL2.

Reduced magnetic exchange is not enough to enable deterministic domain selection: the exchanges on top and bottom surfaces also need to be inequivalent. As a simplified model, we assume that all interlayer exchanges maintain the bulk J^{AFM} except for coupling at one of the two surfaces, which varies as $(1+x)J^{\text{AFM}}$ with $-1 < x < 1$ (Fig. 2, left). In the cartoon, we have chosen the inequivalent exchange to be at the top surface, but analogous arguments also hold when the modified exchange is at the bottom surface, as well as when *both* surface exchanges are inequivalently modified from bulk values (see SM, Sec.3). Now, a state with the BL formed at the surface with modified exchange is lower ($x < 0$) or higher ($x > 0$) in energy than all other BL states, and is thus more or less likely. This breaks the symmetry between transitioning to the domain where the surface having modified exchange has spins up or down (mod. surf \uparrow and mod. surf \downarrow respectively).

We consider $N = 6$ as an example, first through qualitative arguments, followed by a quantitative analysis. For $x < 0$ (Fig. 2(a)), when ramping-down BL3 dominates at fields just below $|H_z^{\text{SF}}|$ (center panel). As $|H_z|$ is further reduced, the AFM domain whose spin at the surface with modified exchange is *opposite* the field direction will be favored (in this case, mod. surf \downarrow), since it differs from BL3 by a single spin flip, whereas reaching the other AFM domain would require flipping all but the

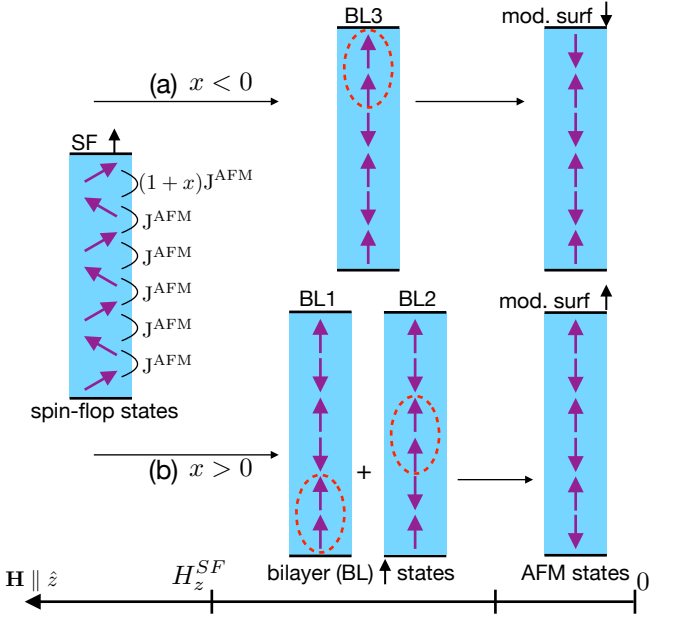


FIG. 2: Transition with decreasing applied field for an asymmetric AFM slab from spin-flop state (left) to one or more intermediate “bilayer” phases (center) to the most probable collinear AFM domain (right) as $H_z \rightarrow 0$, reflecting a ramping-down protocol. Layers 1-5 have interlayer couplings J^{AFM} , while the top coupling is $(1+x)J^{\text{AFM}}$. (a) Transition pathway for $x < 0$. (b) Pathway for $x > 0$.

top spin. The opposite domain mod. surf \uparrow is favored for a ramp-up protocol. For $x > 0$ (Fig. 2(b)), using similar arguments we find opposite domains for a given ramping protocol compared to $x < 0$. These findings can be summarized as follows: at $H_z = 0$, the AFM domain in which the spin on the surface with weaker AFM coupling points opposite the initial field direction is favored. However, as we shall see explicitly, the $x > 0$ and $x < 0$ scenarios are not equivalent since for $x > 0$ two, rather than one, distinct BL locations are low-energy.

We quantify these predictions via “committor functions”, which give the probability that, starting from an initial state A, we end up in possible final state B before hitting possible final state C [15]. We assume sufficiently large uniaxial anisotropy such that all states at fields below $|H_z^{\text{SF}}|$ are collinear, giving 2^N configurations, including the $\frac{N}{2}$ possible BL states and the two AFM domains. We model evolution at fixed H_z and temperature T as a Markov process where a transition from state i to j has probability

$$P(i \rightarrow j) = \begin{cases} \frac{1}{N} \min(1, e^{-\frac{E_j - E_i}{K_b T}}), & d_H(i, j) = 1, \\ 0, & \text{otherwise,} \end{cases} \quad (2)$$

where $d_H(i, j) = 1$ indicates that i and j differ by one spin flip, and the energies are evaluated via Eq. 1.

The committor function to transition from BL state a to collinear AFM domain A , which implicitly takes into account probabilities of all possible transition paths of

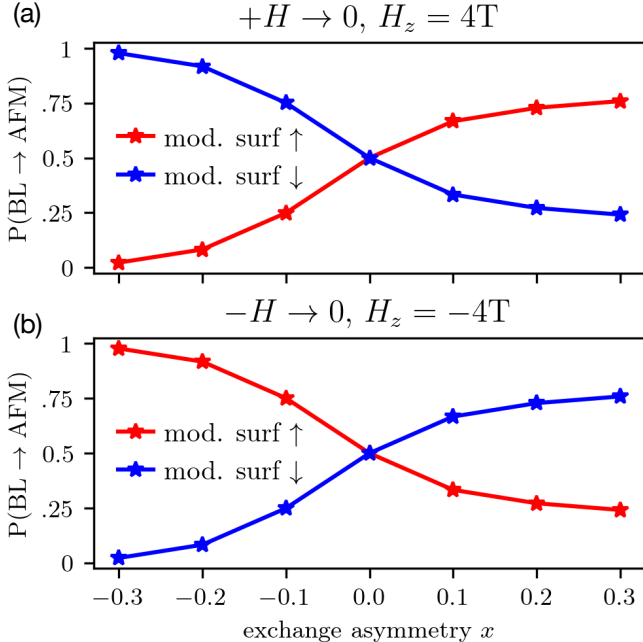


FIG. 3: Total transition probabilities of a six-layer slab for varying surface exchange asymmetry x from any BL state to either domain “mod. surf \uparrow ” or “mod. surf \downarrow ”. (a) evaluated at +4 T reflects a ramping-down field and (b) at -4 T represents ramping-up.

arbitrary length, is given by

$$q_{\text{AFM},A}(\text{BL}, a) = [(\mathcal{I} - \mathcal{Q})^{-1} \mathcal{R}]_{aA}. \quad (3)$$

\mathcal{I} is an identity matrix and \mathcal{Q} (size $(2^N - 2) \times (2^N - 2)$) contains the one-step transition probabilities between all intermediate collinear configurations, *excluding* the two AFM domain states. Diagonal elements enforce total transition probabilities from each state to sum to unity. \mathcal{R} (size $(2^N - 2) \times 2$) contains the one-step transition probabilities from the $(2^N - 2)$ “intermediate” states to one of the two AFM domain states. The row index of Eq. 3 selects the BL state and the column index the AFM domain. To find the total probability of transitioning from any BL state, we compute a Boltzmann-weighted sum;

$$P(\text{BL} \rightarrow \text{AFM}, A) = \sum_{\text{BL}, i} \frac{e^{-E_{\text{BL},i}/K_B T} q_{\text{AFM},A}(\text{BL}, i)}{\sum_{\text{BL}, j} e^{-E_{\text{BL},j}/K_B T}}, \quad (4)$$

which runs over the $N/2$ BL states.

For our calculations we choose $J^{\text{AFM}} = 3$ meV, $|S| = 4.5 \mu_B$, and $K = 1$ meV (see SM, Sec. 6). We evaluate the committors at $T = 5$ K and fields of +4 T (-4 T) to represent ramping-down (ramping-up) protocols; the fields were chosen below the values where the collinear AFM states become lowest in energy, (see SM, Sec. 6). In Fig. 3 we plot both $P(\text{BL} \rightarrow \text{mod. surf} \uparrow)$ and $P(\text{BL} \rightarrow \text{mod. surf} \downarrow)$ versus x for (a) ramping-down and (b) ramping-up protocols. Results are consistent with our qualitative arguments; the AFM domain corresponding to the surface spin with *weaker* AFM exchange pointing *opposite* the initial field sign is consistently favored.

Further, for fixed $|x|$, the bias is stronger for $x < 0$. This is because in one of the likely BL states for $x > 0$, BL2, the bilayer is in the center of the slab, so has appreciable probability to transition to either AFM domain (Fig. 2(b)). In SM Sec. 2, we show that for both signs of x the magnitude $|x|$ required for deterministic domain selection, as well as the asymmetry between $x > 0$ and $x < 0$, increases with the number of layers.

Monte Carlo simulations— To investigate whether the domain-selection mechanism identified in the toy model above remains valid in a more realistic setting, we perform Monte Carlo (MC) simulations of MBT with in-plane periodicity (using 484 spins in each layer in our simulation box; see SM, Sec. 1 for details) and out-of-plane vacuum boundary conditions. We use an in-plane ferromagnetic coupling of $J^{\text{FM}} \sim 1.82$ meV, a uniaxial anisotropy $K = 0.225$ meV, and an out-of-plane $J^{\text{AFM}} = 0.47$ meV, based on the density functional values obtained in Refs. [16, 17] for MBT. We model a relatively thick slab of 48 layers (~ 64 nm): we were unable to converge thicker slabs. We then introduce varying surface exchange anisotropy x and apply ramping-up and ramping-down magnetic fields at $T = 15$ K to test whether this can cause the deterministic selection implied by the MOKE measurements.

Figure 4(a) shows our results. For each ramping protocol, we calculate as a function of field H_z the normalized \hat{z} -component of the Néel vector,

$$L_z = \frac{1}{N|m|} \sum_{k=1}^N m_z^k (-1)^{k-1},$$

where m_z^k is the planar-averaged Mn moment in layer k and $|m| = 3.9 \mu_B$ is the MC saturation magnetization per Mn at 15 K. At each point in Fig. 4(a) we then plot an ensemble average $\langle L_z \rangle$ over five separate MC field-ramping simulations. Thus, $\langle L_z \rangle = +1$ ($\langle L_z \rangle = -1$) means that the mod surf. \downarrow (\uparrow) domain was selected in all five simulations.

The results agree with predictions based on our toy model: for a symmetric slab ($x = 0$), the selected domain is random ($\langle L_z \rangle \sim 0$). For an asymmetric slab with $x = -0.4$ however, the direction of ramping deterministically selects the expected AFM domain (we show results for other x in SM Sec. 4).

More insight can be obtained by studying the switching between the different states, discussed here for the ramp-down protocol. At $H_z^{\text{SF}} \sim 5.25$ T the slab transitions from the spin-flop phase to a BL state with surface spins pointing up (right-hand cartoon in Fig. 4(a) shows the BL state at 5 T). This is followed by a transition to the preferred AFM monodomain at +2.6 T, visible as a kink in $\langle L_z \rangle$. The monodomain is stable until -3.8 T, when the spins on the surface with stronger exchange, still pointing along $+z$, start to align with the field, causing domain wall propagation and eventually switching the sign of $\langle L_z \rangle$ until a collinear BL state with all surface spins pointing down is formed

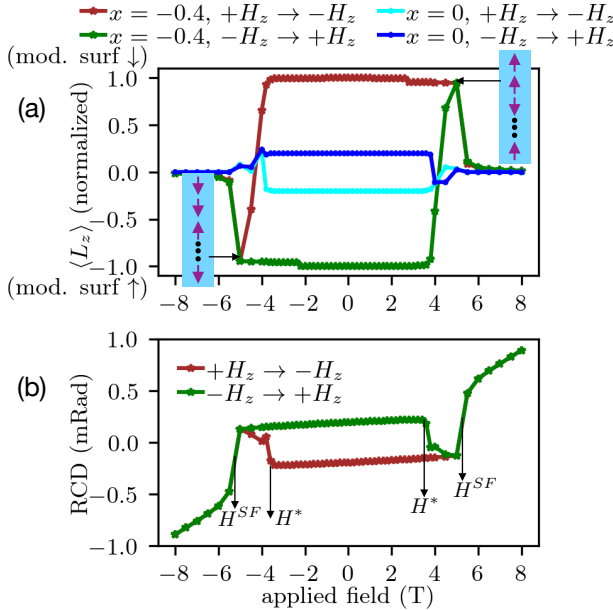


FIG. 4: (a) Ensemble-averaged Néel vector $\langle L_z \rangle$ as a function of applied field based on Monte Carlo (MC) simulations for surface exchange asymmetries $x = 0$ and $x = -0.4$ with ramping-down and ramping-up fields. Cartoons show BL states at ± 5 T, just below $|H_z^{SF}|$, with central spins left out. (b) Simulated RCD measurement using the MC data from $x = -0.4$ in (a). The simulation is done for the photon energy of 2.3eV, using the same dielectric model as in Ref. [11].

at -5 T (left-hand cartoon, Fig. 4(a)). The hysteresis in the Néel vector elucidates the observed MOKE, as described below.

Comparison to MOKE on $MnBi_2Te_4$ — We follow the procedure in Ref. [11] to simulate the MOKE signal arising from the field-dependent magnetic structures found in our MC simulations (SM, Sec. 7). In the experiments the light does not penetrate to the bottom surface; to replicate these conditions in the simulation of a 48-layer slab (about half of experimental thickness), we assume the thickness of each layer to be twice the experimental value, $d = 2.6$ nm.

In Fig. 4(b) we show the simulated reflection circular dichroism (RCD, i.e. imaginary part of MOKE) data based on the MC layer-resolved magnetic structure in Fig. 4(a) for ramping-down (brown) and ramping-up (green). The simulation is done assuming that the surface with stronger exchange is exposed to the light, with the opposite case shown in SM, Sec. 7. Despite the numerous approximations in our MC simulations, the agreement with the experimental RCD (Fig. 2 in Ref. [11]) is quite good. The main qualitative feature, i.e. a hysteretic RCD signal, is reproduced. Moving beyond that, we observe two characteristic fields, $H_z^{SF} = \pm 2.5$ T and $H_z^* = \pm 3.8$ T, which is also a feature of the experiment (although the field values differ). The MC simulations clarify the origin of the two fields: H_z^{SF} and H_z^* correspond to transitioning between

a spin-flop to multidomain BL state, and from an AFM monodomain to a multidomain state, respectively.

From this, we can understand why H_z^{SF} is highly reproducible, while H_z^* is found to vary between experimental studies, and even among different positions on the same sample [11]. H_z^{SF} is set by bulk quantities (AFM exchange and Zeeman energy). In contrast, H_z^* is set by surface properties, and corresponds to a reconfiguration of AFM domains, a process which might be strongly affected by details of defects or strain profiles, induced by distinct sample preparation protocols.

Conclusions— We first comment on this work’s implications for MBT. If sufficient asymmetry exists between magnetic exchange on opposite surfaces of (001)-oriented MBT, our MC simulations show ramp direction-based domain selectivity and field-dependent MOKE in good agreement with the experiment on thick flakes. The surface asymmetry discussed here would also explain the field-tuning of the AFM state in the even-layer thin flakes of MBT, and accounts for variation of characteristic fields for switching of RCD signals across different experimental studies. Crucially, for an idealized symmetric material ($x = 0$) the field-tuning reported in numerous studies would not be possible. We note that several material-specific considerations make surface asymmetry plausible in MBT: details of sample preparation alter observable properties [18], common substrates couple to MBT [19], and the top surface is either interfaced with another material or exposed to air, which leads to oxidation of the top layer [20]. Similar considerations are likely relevant for other van der Waals materials.

Our results further suggest which material platforms may be most promising for realizing this effect. Magnetic field-based domain control is more efficient when at least one surface exhibits weaker—rather than stronger—interlayer AFM exchange than the bulk. Thus, compounds for which AFM coupling is governed by superexchange [21] rather than direct exchange [22] may be better suited to magnetic control, as bond angle changes induced by surface relaxation should weaken superexchange-driven AFM coupling. Further, we note that our MC calculations likely overestimate the anisotropy needed for domain control in a slab of given thickness, due to a limited number of in-plane spins (SM, Sec. 2). On the other hand, the required anisotropy generally increases with slab thickness.

More broadly, the conventional view that AFMs are insensitive to pure magnetic fields should be reexamined in light of the discussed surface effects. When top and bottom surfaces have asymmetric environments, which occurs in many experimental scenarios, the AFM exchanges on the two surfaces will also likely be asymmetric; combined with the generic reduced magnetic exchange at surfaces, this can drive magnetic field-based AFM domain control. We emphasize that our arguments hold for any layered collinear A-type AFM when the field is applied parallel to the easy direction of the

AFM. Given this broad applicability, magnetic field ramping should be a promising option for controlling AFM domains.

We have shown how the enhanced sensitivity of surface spins can be leveraged to achieve deterministic selection of AFM domains when top and bottom surfaces are asymmetric. Going forward, controlled experiments in parallel with quantitative *ab-initio* calculations for different asymmetric AFM slabs need to be carried out in order to assess the baseline materials and experimental conditions for which this mechanism is most promising. We hope that with this work we inspire some readers to join in these crucial followup endeavors.

Acknowledgments

SFW acknowledges funding from Chalmers University of Technology through the department of Physics and the Areas of Advance Nano and Materials Science. VS acknowledges funding from Institute of Science and Technology Austria. Monte Carlo simulations were performed using computing resources from the PDC Center for High Performance Computing. These resources were granted by the National Academic Infrastructure for Supercomputing in Sweden (NAIIS), partially funded by the Swedish Research Council through grant agreement no. 2022-06725.

-
- [1] K. Olejník, T. Seifert, Z. Kašpar, V. Novák, P. Wadley, R. P. Campion, M. Baumgartner, P. Gambardella, P. Němec, J. Wunderlich, J. Sinova, P. Kužel, M. Müller, T. Kampfrath, and T. Jungwirth, Terahertz electrical writing speed in an antiferromagnetic memory, *Sci. Adv.* **4**, eaar3566 (2018).
- [2] V. Baltz, A. Manchon, M. Tsoi, T. Moriyama, T. Ono, and Y. Tserkovnyak, Antiferromagnetic spintronics, *Reviews of Modern Physics* **90**, 015005 (2018).
- [3] S. Y. Bodnar, L. Šmejkal, I. Turek, T. Jungwirth, O. Gomonay, J. Sinova, A. A. Sapozhnik, H. J. Elmers, M. Klaič, and M. Jourdan, Writing and reading antiferromagnetic mn_2au by neél spin-orbit torques and large anisotropic magnetoresistance, *Nat. Commun.* **9**, 348 (2018).
- [4] A. Mahmood, W. Echtenkamp, M. Street, J. L. Wang, S. Cao, T. Komesu, P. A. Dowben, P. Buragohain, H. Lu, A. Gruverman, A. Parthasarathy, S. Rakheja, and C. Binek, Voltage controlled neél vector rotation in zero magnetic field, *Nat. Commun.* **12**, 1674 (2021).
- [5] E. Bousquet, E. Lelièvre-Berna, N. Qureshi, J. R. Soh, N. A. Spaldin, A. Urru, X. H. Verbeek, and S. F. Weber, On the sign of the linear magnetoelectric coefficient in cr_2o_3 , *J. Phys.: Condens. Matter* **36**, 155701 (2024).
- [6] H. Guo, Z. Lin, J. Lu, C. Yun, G. Han, S. Sun, Y. Wu, W. Yang, D. Xiao, Z. Zhu, L. Peng, Y. Ye, Y. Hou, J. Yang, and Z. Luo, Layer-dependent spin-orbit torque switching of neél vector in a van der waals antiferromagnet, *Nat. Commun.* **16**, 8911 (2025).
- [7] D. Ovchinnikov, X. Huang, Z. Lin, Z. Fei, J. Cai, T. Song, M. He, Q. Jiang, C. Wang, H. Li, Y. Wang, Y. Wu, D. Xiao, J.-H. Chu, J. Yan, C.-Z. Chang, Y.-T. Cui, and X. Xu, Intertwined Topological and Magnetic Orders in Atomically Thin Chern Insulator MnBi_2Te_4 , *Nano Letters* **21**, 2544 (2021).
- [8] S. Yang, X. Xu, Y. Zhu, R. Niu, C. Xu, Y. Peng, X. Cheng, X. Jia, Y. Huang, X. Xu, J. Lu, and Y. Ye, Odd-Even Layer-Number Effect and Layer-Dependent Magnetic Phase Diagrams in MnBi_2Te_4 , *Physical Review X* **11**, 011003 (2021).
- [9] J. X. Qiu, C. Tzscheschel, J. Ahn, A. Gao, H. Li, X. Y. Zhang, B. Ghosh, C. Hu, Y. X. Wang, Y. F. Liu, D. Bérubé, T. Dinh, Z. Gong, S. W. Lien, S. C. Ho, B. Singh, K. Watanabe, T. Taniguchi, D. C. Bell, H. Z. Lu, A. Bansil, H. Lin, T. R. Chang, B. B. Zhou, Q. Ma, A. Vishwanath, N. Ni, and S. Y. Xu, Axion optical induction of antiferromagnetic order, *Nat. Mater.* **22**, 583 (2023).
- [10] F. M. Bartram, M. Li, L. Liu, Z. Xu, Y. Wang, M. Che, H. Li, Y. Wu, Y. Xu, J. Zhang, S. Yang, and L. Yang, Real-time observation of magnetization and magnon dynamics in a two-dimensional topological antiferromagnet MnBi_2Te_4 , *Science Bulletin* **68**, 2734 (2023).
- [11] V. Sunko, S. Ahsanullah, V. Jain, S. Weber, S. Kumaran, J. Q. Yan, J. Orenstein, and D. Ovchinnikov, Universal kerr effect in a-type antiferromagnets, *arXiv:2504.16167* (2025).
- [12] S. F. Weber and N. A. Spaldin, Characterizing and overcoming surface paramagnetism in magnetoelectric antiferromagnets, *Phys. Rev. Lett.* **130**, 146701 (2023).
- [13] S. F. Weber, A. Urru, S. Bhowal, C. Ederer, and N. A. Spaldin, Surface magnetization in antiferromagnets: Classification, example materials, and relation to magnetoelectric responses, *Phys. Rev. X* **14**, 21033 (2024).
- [14] P. M. Sass, J. Kim, D. Vanderbilt, J. Yan, and W. Wu, Robust a-type order and spin-flop transition on the surface of the antiferromagnetic topological insulator mnbi_2te_4 , *Phys. Rev. Lett.* **125**, 037201 (2020).
- [15] M. Lindner and F. Hellmann, Stochastic basins of attraction and generalized committor functions, *Phys. Rev. E* **100**, 10.1103/PhysRevE.100.022124 (2019).
- [16] M. M. Otkrov, I. P. Rusinov, M. Blanco-Rey, M. Hoffmann, A. Y. Vyazovskaya, S. V. Eremeev, A. Ernst, P. M. Echenique, A. Arnau, and E. V. Chulkov, Unique thickness-dependent properties of the van der waals interlayer antiferromagnet mnbi_2te_4 films, *Phys. Rev. Lett.* **122**, 107202 (2019).
- [17] M. M. Otkrov, I. I. Klimovskikh, H. Bentmann, D. Estyulin, A. Zeugner, Z. S. Aliev, S. Gaß, A. U. Wolter, A. V. Koroleva, A. M. Shikin, M. Blanco-Rey, M. Hoffmann, I. P. Rusinov, A. Y. Vyazovskaya, S. V. Eremeev, Y. M. Koroteev, V. M. Kuznetsov, F. Freyse, J. Sánchez-Barriga, I. R. Amiraslanov, M. B. Babanly, N. T. Mamedov, N. A. Abdullayev, V. N. Zverev, A. Alfonsov, V. Kataev, B. Büchner, E. F. Schwier, S. Kumar, A. Kimura, L. Petaccia, G. D. Santo, R. C. Vidal, S. Schatz, K. Kißner, M. Ünzelmann, C. H. Min,

- S. Moser, T. R. Peixoto, F. Reinert, A. Ernst, P. M. Echenique, A. Isaeva, and E. V. Chulkov, Prediction and observation of an antiferromagnetic topological insulator, *Nature* **576**, 416 (2019).
- [18] Y. Li, Y. Wang, Z. Lian, H. Li, Z. Gao, L. Xu, H. Wang, R. Lu, L. Li, Y. Feng, J. Zhu, L. Liu, Y. Wang, B. Fu, S. Yang, L. Yang, Y. Wang, T. Xia, C. Liu, S. Jia, Y. Wu, J. Zhang, Y. Wang, and C. Liu, Fabrication-induced even-odd discrepancy of magnetotransport in few-layer MnBi₂Te₄, *Nature Communications* **15**, 3399 (2024).
- [19] G. Li, X. Wu, Y. Gao, X. Ma, F. Hou, H. Cheng, Q. Huang, Y.-C. Wu, M. C. DeCapua, Y. Zhang, J. Lin, C. Liu, L. Huang, Y. Zhao, J. Yan, and M. Huang, Observation of Ultrastrong Coupling between Substrate and the Magnetic Topological Insulator MnBi₂Te₄, *Nano Letters* **22**, 3856 (2022).
- [20] A. R. Mazza, J. Lapano, H. M. MeyerIII, C. T. Nelson, T. Smith, Y.-Y. Pai, K. Noordhoek, B. J. Lawrie, T. R. Charlton, R. G. Moore, T. Z. Ward, M.-H. Du, G. Eres, and M. Brahlek, Surface-Driven Evolution of the Anomalous Hall Effect in Magnetic Topological Insulator MnBi₂Te₄ Thin Films, *Advanced Functional Materials* **32**, 2202234 (2022).
- [21] P. W. Anderson, New approach to the theory of superexchange interactions, *Phys. Rev.* **115**, 2 (1959).
- [22] J. B. Goodenough, Direct cation-cation interactions in several oxides, *Phys. Rev.* **117**, 1442 (1960).
- [23] B. Skubic, J. Hellsvik, L. Nordström, and O. Eriksson, A method for atomistic spin dynamics simulations: Implementation and examples, *J. Phys.: Condens. Matter* **20**, 315203 (2008).
- [24] W. Hergett, N. Bouldi, M. Jonak, C. Neef, C. Ritter, M. Abdel-Hafiez, F. Seewald, H. H. Klauss, M. W. Haverkort, and R. Klingeler, Quasi-two-dimensional magnetism and antiferromagnetic ground state in Li₂FeSiO₄, *Phys. Rev. B* **111**, 024414 (2025).
- [25] P. J. Feibelman, Relaxation of hcp(001) surfaces: A chemical view, *Phys. Rev. B* **53**, 13740 (1996).
- [26] M. W. Finnis and V. Heine, Theory of lattice contraction at aluminium surfaces, *J. Phys. F: Metal Phys.* **4**, L37 (1974).
- [27] F. Hendriks and M. H. D. Guimarães, Enhancing magneto-optic effects in two-dimensional magnets by thin-film interference, *AIP Advances* **11**, 035132 (2021).
- [28] M. Köpf, J. Ebad-Allah, S. H. Lee, Z. Q. Mao, and C. A. Kuntscher, Influence of magnetic ordering on the optical response of the antiferromagnetic topological insulator MnBi₂Te₄, *Physical Review B* **102**, 165139 (2020).

SUPPLEMENTARY MATERIAL

1. Monte Carlo calculations for MnBi_2Te_4

For our simulations of MBT, we use Monte Carlo (MC) as implemented in the spin dynamics package Up-ASD [23]. We take the hexagonal setting of MBT (Fig. S1) as the input structure, and use supercells of $22 \times 22 \times N$, where N is the number of out-of-plane layers. The correspondingly modest number of in-plane spins (484 per layer), is necessary for the 48-layer results shown in the main text due to computational overhead, and we keep the same in-plane size MC simulations of a six-layer MBT slab shown in SM Sec. 5 to directly compare with the 48 layer case. We use periodic boundary conditions in the in-plane directions and vacuum boundary conditions along the hexagonal (001) direction to mimic the experimental crystal orientation.

We take directly the spin Hamiltonian parameters reported in Refs. [16] and [17] which were obtained from density functional calculations. We include up to third nearest neighbor in-plane Heisenberg exchange, with $J_1 = -1.86$ meV, $J_2 = 0.05$ meV and $J_3 = -0.01$ meV (where $J < 0$ indicates a ferromagnetic coupling and $J > 0$ indicates an antiferromagnetic coupling). This yields an effective ferromagnetic in-plane coupling of $J^{\text{FM}} \sim -1.82$ meV as mentioned in the main text. For simplicity, for the out-of-plane AFM coupling we use a single effective nearest-neighbor exchange $J^{\text{AFM}} = \sum_{i,\perp} J_i^\perp = 0.47$ meV, where the sum is over all out-of-plane nearest neighbors. We use a uniaxial out-of-plane single-ion anisotropy of 0.225 meV/Mn. We take $S_i = 4.5 \mu_B$ as the zero-Kelvin value of the Mn magnetic moments (based on DFT calculations we performed for Ref. [11]). This is the number which is used as the baseline to renormalize the moment magnitudes at finite temperatures in the MC simulations.

As an aside, we note that when we calculate the heat capacity using an MC simulation of bulk MnBi_2Te_4 with 24200 spins (Fig. S2), we find a Néel temperature of $T_N \sim 40$ K based on the peak. This overestimates the experimental Néel temperature $T_N \sim 25$ K of MBT, indicating an overestimation of the experimental exchange values. This is consistent with the fact that the critical field values in our MC simulations are all slightly higher than in experiments Ref. [11, 17]. More surprisingly, our determination of T_N is also in disagreement with the estimate of Ref. [17], from which we obtain our spin Hamiltonian parameters; based on calculation of the susceptibility, they find $T_N \sim 25$ K, very close to experiment. We assume that the discrepancy stems partially from the fact that we compress the out-of-plane coupling into a single effective $J^{\text{AFM}} = \sum_{i,\perp} J_i^\perp = 0.47$ meV for simplicity in making the main point of our work, which is the deterministic selection of AFM domains via magnetic fields when surface exchanges are inequivalent. On the other hand, Ref. [17] explicitly takes into account up to 70 magnetic shells of out-of-plane nearest neighbors. Moreover,

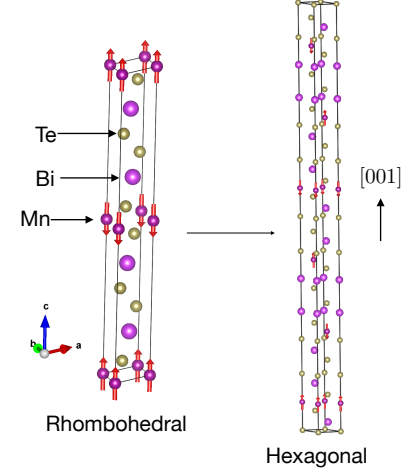


FIG. S1: Crystal structure of MnBi_2Te_4 with the ground-state A-type antiferromagnetic ordering in the primitive rhombohedral setting (left) and in the hexagonal setting (right) which we use as the input cell for our Monte Carlo simulations. We model the (001) hexagonal surface cut, reflecting the experimental surface crystal orientation in Ref. [11], by using vacuum boundary conditions along the (001) direction and periodic in-plane boundary conditions. The picture of the hexagonal structure shows six Mn layers.

there are known issues in accurately determining T_N in quasi-2D AFMs such as MnBi_2Te_4 due to short-range correlations that can occur well above the true T_N [24]. A careful determination of T_N using e.g. Binder cumulants or finite-size scaling in Monte Carlo is beyond the scope and purpose of the present work.

For the field-ramping simulations for both 48-layer and six-layer MBT slabs, we use a constant temperature of 15 K and apply an external magnetic field parallel to the out-of-plane easy axis. We start at 8 T (-8 T) for ramping down (ramping up) simulations, which is above the spin-flop field $|H_z^{\text{SF}}| = 5.25$ T based on our simulations. We initialize a random initial spin configuration for the first field values. After a full MC run at constant field value, we decrease (increase) the field for ramping-down (ramping-up) protocols and run another MC simulation at a new field value, using the final spin configuration from the previous field run as our starting configuration. We ramp the field in steps of 0.5 T between ± 4 T to ± 8 T and in steps of 0.2 T between -4 T and $+4$ T.

At each field value, the Néel vector (Eq. 5 in the main text) is calculated using the \hat{z} component of the average sublattice magnetizations m_z^k for each layer k , calculated as

$$m_z^k = \frac{1}{N_{\text{cells}}} \sum_{j=1}^{N_{\text{cells}}} m_{z,j}^k. \quad (\text{S1})$$

Here, N_{cells} is the the number of unit cells (and spins per layer) in the simulation box, $22 \times 22 = 484$. We additionally average the layer magnetization in Eq. S1 over 200,000 MC steps, starting the average after

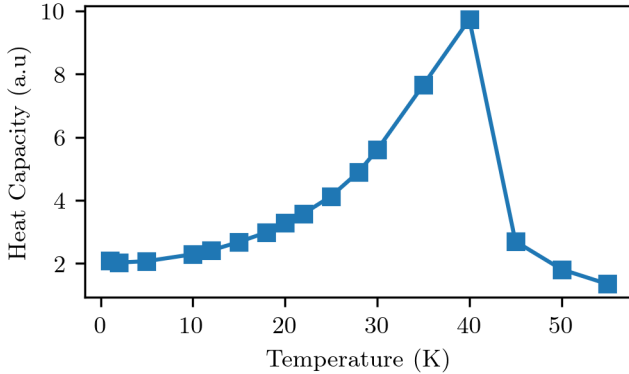


FIG. S2: Heat capacity as a function of temperature from a Monte Carlo simulation of bulk MnBi_2Te_4 . using the spin Hamiltonian parameters of Ref. [17].

500,000 initial steps which bring the system into equilibrium at each field value. Lastly, we do an ensemble average over five independent MC calculations to get the final values of m_z^k which go into calculation of the field-dependent ensemble-averaged Néel vector $\langle L_z \rangle$ as well as the MOKE simulations. The relatively few ensemble averages, necessary due to the long run-time of the simulations, result in rough statistics, but are sufficient to make our points.

2. Dependence of domain selection robustness on magnetic exchange, thickness and temperature

It is important to understand how the robustness of deterministic domain selection for fixed surface exchange asymmetry and ramping direction changes when other parameters are varied. In Fig. S3, we evaluate the committor functions for transitioning from the intermediate bilayer (BL) phase to either of the two collinear AFM domains where we vary (a) temperature; (b) J^{AFM} ; and (c) slab thickness. We show results for both $x < 0$ (purple) and $x > 0$ (green) exchange anisotropy of the top surface with a consistent magnitude $|x| = 0.3$. The positive magnetic field at which the energies going into the committor are calculated is $H_z = +4$ T for $J^{\text{AFM}} = 3$ meV (the same field magnitude used to calculate the committors in the main text, see SI S.6 for further details) and it is scaled proportionally when J^{AFM} is varied in Fig. S3(b). We show only the domains which are favored for this ramping direction. They correspond to the mod. surf \downarrow domain for $x = -0.3$ and the mod. surf \uparrow domain for $x = +0.3$.

We give the equations for the committor functions from the main text here again for convenience: one-step transition probabilities related by single spin flips along a Markov chain for an N -layer slab are given by

$$P(i \rightarrow j) = \begin{cases} \frac{1}{N} \min\left(1, e^{-\frac{E_j - E_i}{K_B T}}\right), & d_H(i, j) = 1, \\ 0, & \text{otherwise,} \end{cases} \quad (\text{S2})$$

where $d_H(i, j) = 1$ indicates that i and j differ by one spin flip. These one-step probabilities go into the individual committor functions $q_{\text{AFM}, A}(\text{BL}, a)$ to transition for a specific BL state to a specific AFM domain state. Finally, to get the total probability $P(\text{BL} \rightarrow \text{AFM}, A)$ to transition from any of the possible BL states to a given AFM domain A , we compute the weighted sum

$$P(\text{BL} \rightarrow \text{AFM}, A) = \sum_{\text{BL}, i} \frac{e^{-E_{\text{BL}, i}/K_B T} q_{\text{AFM}, A}(\text{BL}, i)}{\sum_{\text{BL}, j} e^{-E_{\text{BL}, j}/K_B T}}, \quad (\text{S3})$$

which is plotted in Fig. S3 and Fig. 3 of the main text.

For all three plots, the trend is the same for both signs of anisotropy, but the details vary. We first consider the committors as a function of varying temperature in Fig. S3(a). For both $x < 0$ and $x > 0$ the probability to transition to the favored domain decreases with increasing temperature since transitions to the lower-energy states are suppressed by the Boltzmann factor $\exp(1/K_B T)$, both in the intermediate, single spin flip transitions (Eq. S2) and in the overall weighted committor (Eq. S3). However, the effect is stronger in the $x < 0$ case. We can understand this by noting that for $x < 0$, Boltzmann weight in Eq. S3 corresponding to the BL state with the bilayer at the surface with modified exchange dominates over all other BL states. For $x > 0$ on the other hand, $\frac{N}{2} - 1$ possible BL positions with equal likelihood contribute significantly to the overall transition probability, so the temperature dependence in Eq. S3 less strongly re-weights the energetically favorable and unfavorable BL states than in the $x < 0$ case.

In Fig. S3(b), we plot Eq. S3 as a function of interlayer AFM coupling J^{AFM} , given in meV. The transition probability for the favored domain increases with J^{meV} . This is because the energy lowering in going from ferromagnetically coupled bilayers to AFM-coupled layers increases with J^{meV} , and spin-flips leading to the AFM state (Eq. S2) thus become more likely.

We note that the increase in domain selection asymmetry with increasing J^{AFM} is closely tied to the reason that we had to use a large J^{AFM} ($J^{\text{AFM}} = 3$ meV) in evaluating the committor functions in order to get nearly definite probability for the favored domain in Fig. 3 of the main text (this is also clear from Fig. S3(b)). Recall that our toy model used to evaluate Eq. S3 assumes only a single spin per layer. In contrast, a (001)-oriented crystal of MnBi_2Te_4 has many more in-plane spins, which are coupled ferromagnetically via $J^{\text{FM}} \sim -1.82$ meV, than out-of-plane layers coupled by a relatively weak $J^{\text{AFM}} \sim 0.47$ meV. Thus, at temperatures where the out-of-plane AFM coupling becomes relevant, the layers are fairly rigidly locked in their in-plane FM ordering, and can be thought of as macropins with total magnetization $m_{\text{layer}} \sim N_{\parallel} \times m_{\text{Mn}}$ with N_{\parallel} the number of spins per layer and m_{Mn} the magnetic moment of a single Mn ion. Thus, the energy lowering to align layers antiferromagnetically grows roughly as $\Delta E \sim N_{\parallel} J^{\text{AFM}}$. Therefore, the effective J^{AFM} which determines the cer-

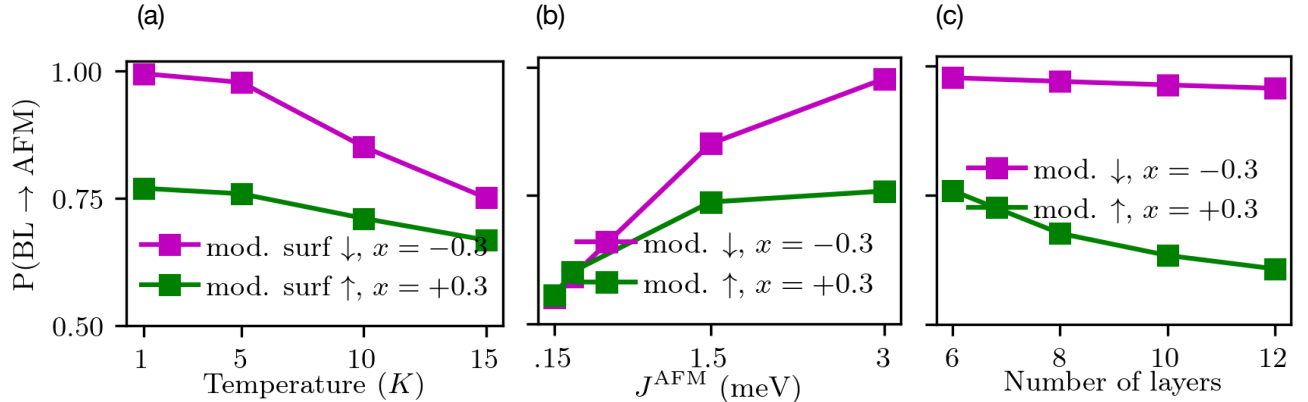


FIG. S3: Committor functions showing summed probability to transition from any of the bilayer states to one of the two AFM domains as function of (a) temperature; (b) J_{AFM} and (c) number AFM-coupled layers in the slab. We show results for $x < 0$ (purple) and $x > 0$ (green) with $|x| = 0.3$, and we only plot the committor the AFM domain which is favored for each sign of x for the ramping down protocol assumed in the calculations. (a) and (b) are calculated with a six-layer slab. The temperature is 5K when it is not being varied, and $J_{\text{AFM}} = 3\text{meV}$ when not being varied. Uniaxial anisotropy K and magnetic moment value $S_i = 4.5\mu_B$ are kept constant in all cases.

tainty of domain selection scales with the number of in-plane spins. This is why with our MC simulations of MBT using ~ 500 in-plane spins, we can get definitive domain selection using a smaller J_{AFM} than one would assume from the spin-chain toy model considered in Fig. S3(b). This also indicates encouragingly that for the experimental situation in Ref. [11] where the number of in-plane spins for MBT is much larger than in our MC simulations, the magnitudes of surface exchange asymmetry required to get deterministic domain selection for both signs of x are almost certainly smaller than what we find in this work.

In Fig. S3(c) we plot Eq. S3 as a function of number of out-of-plane layers (the matrix sizes are too large for efficient evaluation of the committor function beyond 12 layers). For both $x < 0$ and $x > 0$ the robustness of deterministic domain selection decreases with increasing number of layers. This is because the number of BL states with the BL, or domain wall, in the interior of the slab increases with increasing layer number. These states have similar probability to transition to either AFM domain, so they suppress the overall robustness of deterministic selection based on the field-ramping direction. For surface exchange asymmetry with $x < 0$ however, the decrease in domain selection robustness is much weaker as a function of layer number, since the central bilayer states are higher energy and thus still relatively unlikely compared to the state where the BL is at the surface with the weaker exchange. For $x > 0$ on the other hand, all the central BL states are low-energy compared to the state with the BL at the more strongly AFM surface. Thus, an increase in these low-energy states with increasing layer number strongly decreases probability for the favored AFM domain to be selected.

Finally, we mention how the robustness of deterministic domain selection probability depends on the uniaxial single-ion anisotropy K . Because we only consider

collinear states in the Ising-like toy model used in our committor functions (in order to restrict the state space to a tractable size), evaluation of Eqs. S2 and S3 yields no information about the barriers for spin rotation set by K . However, it is intuitively clear that as the single-ion anisotropy along the out-of-plane direction \hat{z} increases, the energy cost to rotate spins from $+\hat{z}$ to $-\hat{z}$ or vice versa will also increase. Thus, deterministic domain selection becomes more difficult with increasing K . This is apparent from tests we have run in our Heisenberg-like MC simulations which require rotations from the easy axis in order to flip spins in MBT; namely, if K is much greater than J_{AFM} we start to see a decrease in domain selection asymmetry for a given ramp direction.

Lastly, we note that at smaller relative K values, when the uniaxial anisotropy is much smaller than J_{AFM} , the energetically favorable bilayer states are not fully collinear as in our simplified toy model for evaluating committor functions, or in the case of MBT where K and J_{AFM} are comparable. Instead, we have verified with MC simulations that when $|K| \ll |J_{\text{AFM}}$, there is still a region of fields below the spin-flop field where top and bottom surface spins are both pinned parallel to the applied field, enforcing a multidomain state. However, the interior spins still retain a significant in-plane canting in this case.

3. Committor functions for $J_{\text{bottom}}^{\text{AFM}} \neq J_{\text{bulk}}^{\text{AFM}}$

In the main text, we use a simplified model of surface exchange asymmetry where the bottom-most interlayer exchange between layers 1 and 2 keeps the bulk value J_{AFM} , and only the top exchange between layers N and $N - 1$ varies. In reality, however, atoms at any vacuum-terminated surface or interface will typically relax, or even reconstruct, with respect to their bulk positions

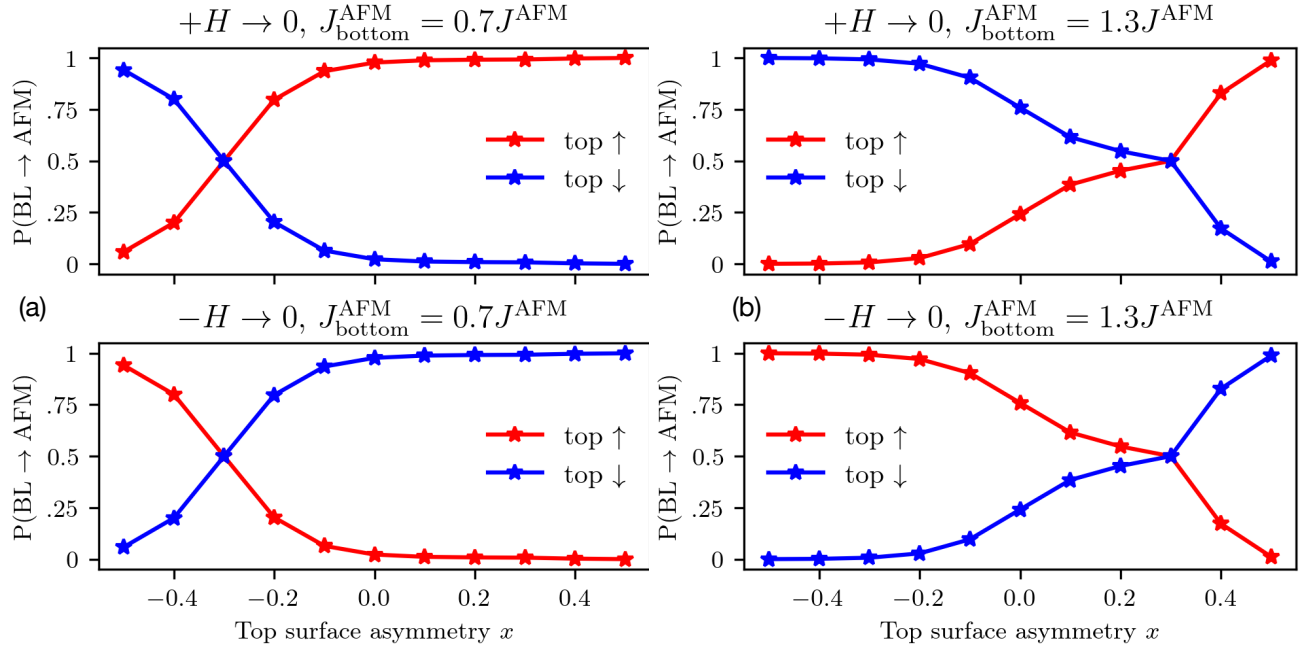


FIG. S4: Committor functions showing summed probability to transition from any of the bilayer states to one of the two AFM domains as function of top layer surface asymmetry x . All interior interlayer couplings are set to $J^{\text{AFM}} = 3$ meV, just like Fig. 3 in the main text. In contrast to the main text, here the bottom surface exchange is also different from the bulk interlayer couplings, such that in (a) it is fixed at $x_{\text{bottom}} = -0.3$ ($J_{\text{bottom}}^{\text{AFM}} = 0.7J^{\text{AFM}}$) and in (b) it is fixed at $x_{\text{bottom}} = +0.3$ ($J_{\text{bottom}}^{\text{AFM}} = 1.3J^{\text{AFM}}$).

as a result of the altered chemical environment [25, 26]. Thus, in general *both* top and bottom surface exchanges will be modified from the bulk J^{AFM} . In Fig. S4 we calculate committor functions (Eq. 4 in the main text) to transition from the BL phase to either the top surf \uparrow (red, called mod. surf \uparrow in main text) or top surf \downarrow (blue, called mod. surf \downarrow in the main text) AFM domain at a positive (ramp-down) or negative (ramp-up) H_z value where the transition is likely to occur based on the relative energetics of BL states and AFM states (see S.6). Ramp-down cases are shown in the top panels, and ramp-up cases are in the bottom panels. Analogously to Fig. 3 in the main text, we plot the committors for both AFM domains as a function of varying top surface exchange asymmetry x , but now we fix the bottom interlayer exchange to either (a) $J_{\text{bottom}}^{\text{AFM}} = 0.7J^{\text{AFM}}$ (corresponding to $x_{\text{bottom}} = -0.3$) or (b) $J_{\text{bottom}}^{\text{AFM}} = 1.3J^{\text{AFM}}$ ($x_{\text{bottom}} = +0.3$). We use the same parameters as in the committor calculations of the main text, namely $J^{\text{AFM}} = 3$ meV, $K = 1$ meV, a temperature of 5K, and applied fields of +4 T (-4 T) for ramping-down (ramping-up) calculations.

It is apparent in both cases that the preferred domain for a given ramping protocol follows the same *relative* logic as for the situation of a single surface exchange differing from the bulk, shown in Fig. 3 of the main text. Specifically, the domain with top surface spins pointing opposite (parallel) to the initial sign of H_z in the ramping protocol is favored when the top surface exchange is weaker: $x_{\text{top}} < x_{\text{bottom}}$ (stronger: $x_{\text{top}} > x_{\text{bottom}}$) than the bottom surface exchange. Note that now,

the crossover points where there is equal probability to transition to either domain occur not when the top surface x is zero, but instead when $x_{\text{top}} = x_{\text{bottom}}$.

Thus, our arguments in the main text are robust for more realistic models of surface exchange asymmetry where $J_{\text{top}}^{\text{AFM}} \neq J_{\text{bottom}}^{\text{AFM}}$ and both surface exchanges differ from the bulk-like J^{AFM} of the central layers. The only caveat is that both x_{bottom} and x_{top} should lie within -1 and $+1$ such that the effective exchanges for both surfaces are less than the effective exchanges $2J^{\text{AFM}}$ of central layers, causing the bilayer phase with pinned surface spins to be stabilized at intermediate fields.

As a final comment, the asymmetry in deterministic domain selection for weaker, $x < 0$, compared to stronger, $x > 0$ surface exchange relative to the bulk interlayer J^{AFM} is also apparent in this more realistic surface model. In Fig. S4(a) where $x_{\text{bottom}} = -0.3$, we already get the favored AFM domain for both ramping protocols with nearly unit probability when $x_{\text{top}} = 0$, implying a relative asymmetry between top and bottom surfaces of 0.3. In Fig. S4(b) in contrast, where $x_{\text{bottom}} = +0.3$, we do not get definitive domain selection until $x_{\text{top}} \approx -0.2$, implying that a relative surface asymmetry of 0.5 is required. Interestingly, from Fig. S4(b), we see that once x_{top} is more positive than x_{bottom} , the domain selection asymmetry grows very rapidly with increasing x_{top} . From inspection of the the committor functions from individual bilayer states to specific domains (as opposed to the weighted sum over all possible bilayer states calculated in the figure), this

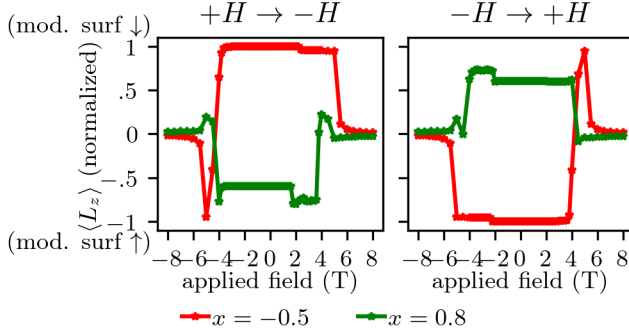


FIG. S5: \hat{z} -component of normalized Néel vector L as a function of applied field based on Monte Carlo (MC) simulations of 48-layer MBT for surface exchange asymmetries $x = -0.5$ and $x = 0.8$.

appears to stem from a strongly suppressed probability for states with central bilayer positions to transition to the disfavored domain. This is because this transition requires an intermediate step where the bilayer moves to the top surface which has stronger AFM coupling than the bottom surface. We caution that we have not yet observed this phenomenon in our Monte Carlo simulations, so the trend should be taken with a grain of salt until follow-up MC simulations are performed with varying top and bottom surface exchanges.

4. Monte Carlo simulations for 48-layer MnBi₂Te₄ with other x values-

In the main text, our goal was to demonstrate that finite asymmetry in magnetic exchange between top and bottom surfaces can lead to deterministic domain selection via magnetic fields as observed experimentally in Ref. [11]. Thus, in Fig. 4 of the main text we only show the ensemble-averaged AFM order parameter $\langle L_z \rangle$ as a function of applied field for the smallest magnitude of surface exchange asymmetry ($x = -0.4$) which we found to lead to selection of the same domain for a fixed ramping direction in all MC simulations. Here in Fig. S5 we plot $\langle L_z \rangle$ versus H_z for ramping-down (left) and ramping-up (right) for a larger negative value of asymmetry, $x = -0.5$, and for a positive surface exchange asymmetry $x = 0.8$.

Qualitatively, $\langle L_z \rangle$ vs. H_z for $x = -0.5$ is very similar to the result for $x = -0.4$ in Fig. 4(a) of the main text. Transitions between spin-flop and multidomain BL states occur at $H_z^{SF} = \pm 5.25$ T. For ramping-down, the transition from the energetically favorable BL \uparrow state (with the BL at the surface with weaker exchange) to the mod. surf \downarrow domain occurs at 2.2 T, which is slightly lower than the 2.6 T value for $x = -0.4$. This is because the larger value of x in Fig. S5 means that the ferromagnetically coupled BL is energetically favored compared to AFM interlayer coupling until lower applied field values, so the surface spin with weaker

AFM exchange resists flipping against the field until a lower field strength. On the other hand, the field at which the mod. surf \downarrow monodomain begins to transition to a BL \downarrow state for a ramping-down protocol is -3.8 T, unchanged from the corresponding field for $x = -0.4$ in the main text. This is because this transition requires flipping the bottom spin of the slab to align with the negative field, which for our model of surface asymmetry always has an AFM exchange fixed to the bulk J^{AFM} .

The results for $x = 0.8$ differ more dramatically from the results in the main text. First, we note that as expected we do get the opposite preferred domain for $x > 0$ compared to $x < 0$ for a fixed ramping direction. However, there is more oscillation in $\langle L_z \rangle$ as the system transitions from the spin-flop phase to the BL phase to an AFM monodomain phase, because unlike in the $x < 0$ case, the bilayers locate in different positions across the five MC ensembles we use for averaging. Thus, the probability to reach the preferred mod. surf \uparrow (for ramping-down) or mod. surf \downarrow (for ramping-up), and thus the critical field at which it occurs, differs across the simulations in the ensemble. On the other hand, the critical field H_z^* at which the AFM monodomain begins to transition to a BL state with surface spins in the opposite direction is quite consistent at $H_z^* \sim \pm 4.5$ T. This is because the field value of this second transition involves flipping of the bottom surface spin to align with the field and is set simply by the relative strengths of J^{AFM} and H_z rather than a probabilistic motion and “expelling” of the BL in the BL \rightarrow AFM monodomain transition.

Perhaps most notably, we see that for $x = 0.8$, $\langle L_z \rangle$ at $H_z = 0$ only reaches about 0.6 in magnitude; this means that in our ensemble averages the AFM domain *opposite* to that expected by our statistical mechanics arguments is selected about 2/5 of the time. This would seem to imply that for such a thick slab of MBT, completely deterministic domain control via field ramping cannot be achieved when the surface exchange is more strongly AFM than the bulk J^{AFM} . However, recall first that if we compare Figs. 3 and Fig. S4 in SI 3, the robustness for deterministic domain selection with a given surface having stronger AFM exchange than J^{AFM} becomes much stronger if the opposite surface has slightly *weaker* AFM exchange, which is plausible for asymmetric growth conditions and environments, or defects. Secondly and likely more importantly, we discussed in SI 2 that in AFMs such as MBT with strong in-plane FM coupling (such that the layers behave as rigid macrospins), increasing the number of in-plane spins reduces the surface exchange anisotropy required for deterministic selection. Thus $|x|$ (of either sign) needed for deterministic domain selection in experiments is almost certainly lower than that needed for the slab in our MC simulations.

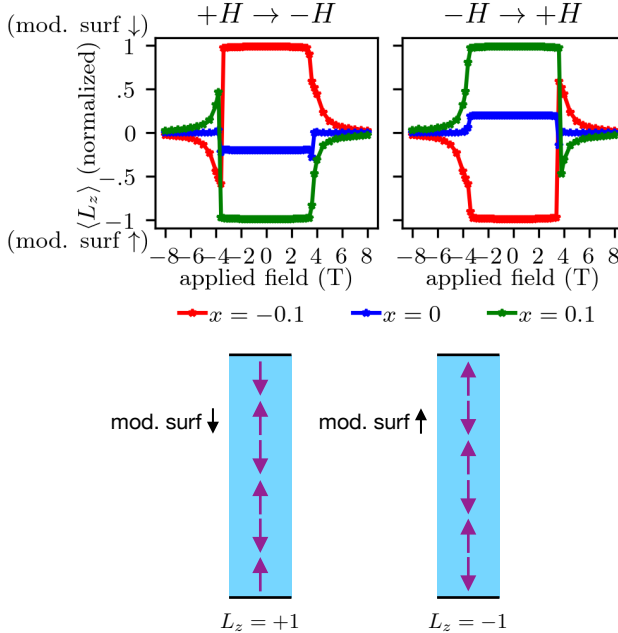


FIG. S6: \hat{z} -component of ensemble-averaged normalized Néel vector $\langle L_z \rangle$ as a function of applied field based on Monte Carlo (MC) simulations for varying surface exchange asymmetry x for a six-layer slab of MBT. Left-hand side is a ramping down simulation, and right-hand side is a ramping up simulation. Bottom cartoons show the correspondence between the sign of $\langle L_z \rangle$ and the “mod. surf ↑” and “mod. surf ↓” domains using our convention.

5. Monte Carlo simulations for six-layer MnBi_2Te_4 slab

For our MC simulations of MBT in the main text, we used as thick a slab as possible to mimic the bulk-like sample in Ref. [11]. In Fig. S6 we compute the normalized ensemble-averaged Néel vector for a six-layer slab of MBT, corresponding to a thin film of about 8nm. The most obvious difference between results for the bulk-like 48-layer slab in the main text (Fig. 4) and SI 4, and the thin film in Fig. S6 is that we get deterministic domain selection ($\langle L_z \rangle = \pm 1$) based on field-ramping direction at much smaller levels of surface anisotropy x for a six-layer slab than the 48-layer slab. Specifically, we have consistent selection of opposite domains for a fixed ramping direction for $x = -0.1$ and $x = 0.1$ respectively. The fact that we do not see the expected increase in required anisotropy magnitude for $x > 0$ relative to $x < 0$ to get deterministic control is likely due either to our relatively crude statistics, or an even smaller critical value of x for $x < 0$ which we did not check.

In stark contrast to the small anisotropy values needed in Fig. S6, for the 48-layer slab studied in the main text, we first get $\langle L_z \rangle = \pm 1$ at $H_z = 0$ for $x = -0.4$, and with our relatively small in-plane slab we never get fully deterministic selection for $x > 0$. As we argued and showed explicitly in SI 2 via evaluation of committor functions, this trend is consistent with the fact that thicker AFMs

have more possible central bilayer positions that have similar probability to transition to either domain. As a result, a larger surface exchange anisotropy x is required for thicker slabs in order to overcome this suppression in deterministic selection.

Other than the difference in necessary values of surface exchange anisotropy, the evolution of magnetic order as a function of H_z is qualitatively similar for thin (six-layer) and thick (48-layer) MBT slabs based on our MC simulations. For $x = 0.1$ and ramping-down, the $\text{BL} \uparrow$ state \rightarrow AFM and AFM \rightarrow $\text{BL} \downarrow$ state transitions occur at 3.6T and -3.8T respectively in Fig. S6 (for ramping-up, the field signs are just swapped). For $x = -0.1$ and ramping down, the $\text{BL} \uparrow$ state \rightarrow AFM and AFM \rightarrow $\text{BL} \downarrow$ state transitions occur at 3.4T and -3.6T respectively. In both cases the critical fields for $\text{BL} \rightarrow$ AFM and AFM \rightarrow BL transitions are nearly symmetric about $H_z = 0$, in contrast to the 48-layer slab at $x = -0.4$ where the two directions of the transitions were fairly asymmetric (|2.6|T for $\text{BL} \rightarrow$ AFM and |3.8|T for AFM \rightarrow BL). This is simply because the surface exchange asymmetry needed for the thicker slab is much larger, and (as discussed in the previous section), since the two directions of the transition necessarily involve flipping opposite surface spins, the critical fields for $\text{BL} \rightarrow$ AFM and AFM \rightarrow BL become less symmetric about zero as the surface exchange asymmetry x increases.

6. Energetics for bilayer, AFM and spin-flop states

In the main text, we argued that for realistic AFM crystals with vacuum-terminated surfaces, spins at the surface have a reduced AFM exchange compared to sublattices in the bulk due to truncation of nearest neighbors. This implies that there is a range of fields for which a multi-domain bilayer (BL) state characterized by top and bottom surface spins pinned parallel to the direction of an applied field H_z and a ferromagnetically coupled bilayer (equivalently, a domain wall) somewhere in the slab is energetically preferable to both the spin-flop phase and the monodomain AFM phase. Here we show this explicitly by plotting the energy as a function of H_z for different magnetic configurations in our toy-model Hamiltonian (Eq. 1 in the main text). For convenience, we repeat the Hamiltonian here, which is

$$E = E_0 + J^{\text{AFM}} \sum_{ij} \hat{e}_i \cdot \hat{e}_j - K \sum_i (\hat{e}_i \cdot \hat{z})^2 - C \sum_i (S_i)^z H_z. \quad (\text{S4})$$

As in the main text, the sum is over magnetic atoms in the unit cell (with one atom per layer); \hat{e}_i is the unit vector parallel to the magnetic moment on site i ; S_i is the magnetic moment of site i in μ_B , and $C = 0.058 \frac{\text{meV}}{\mu_B \text{T}}$ converts $\mu_B \cdot \text{T}$ to eV.

We take the same parameters which we used to evaluate the committors in Fig. 3 of the main text, namely

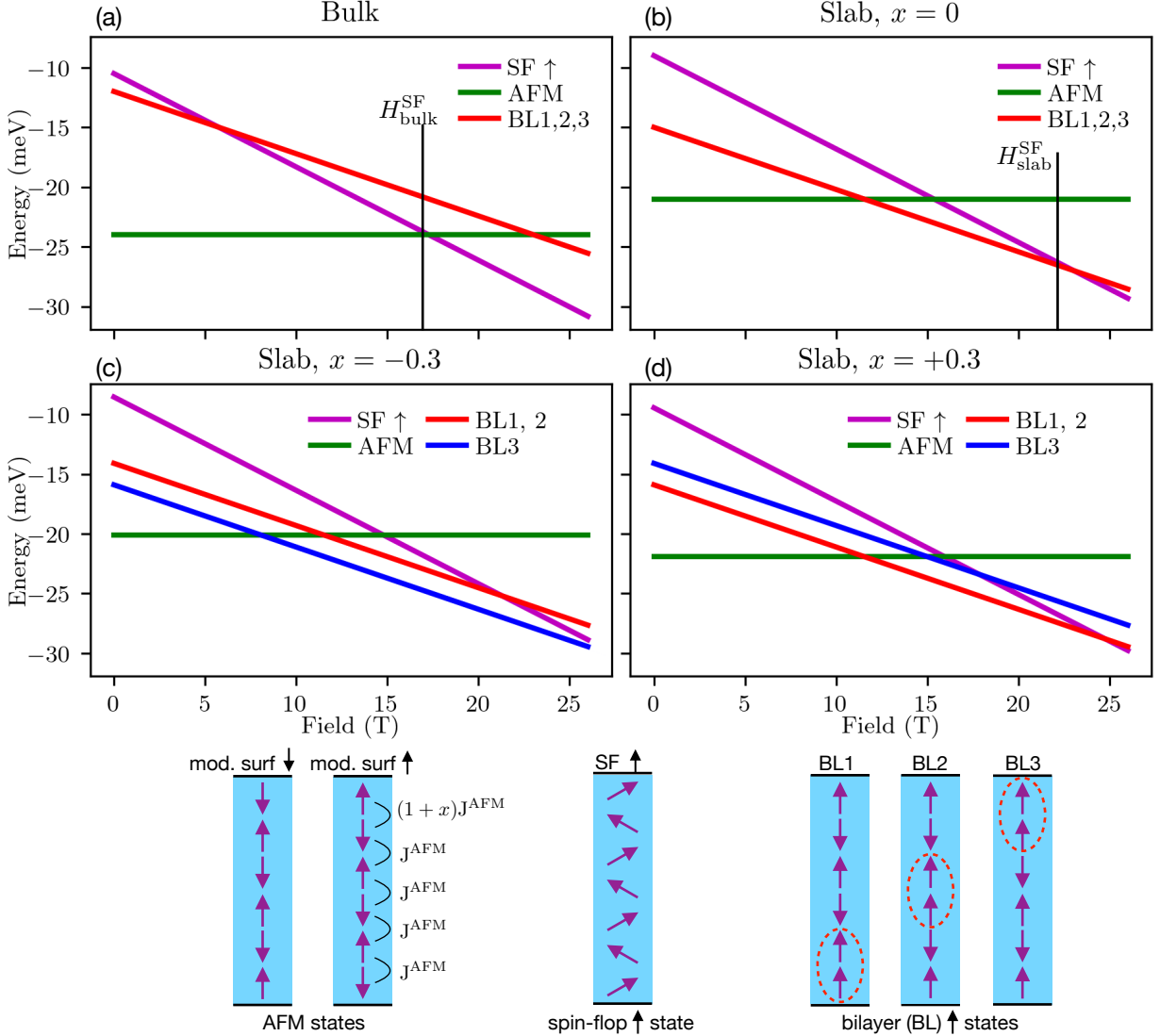


FIG. S7: Energy of a six-layer slab from Eq. S4 versus field H_z for the magnetic configurations in the bottom panel; note that the two AFM states, on the left of the bottom panel, are always energetically degenerate. Layers 1-5 have interlayer couplings J^{AFM} , while the top coupling is $(1+x)J^{\text{AFM}}$. (a) Periodic bulk AFM. (b) Symmetric vacuum-terminated slab ($x = 0$). (c) Asymmetric slab with $x = -0.3$ ($J_{\text{top}} = 0.7J^{\text{AFM}}$). (d) Asymmetric slab with $x = +0.3$ ($J_{\text{top}} = 1.3J^{\text{AFM}}$).

$N = 6$ for the number of AFM-coupled layers, $J^{\text{AFM}} = 3$ meV, $|S| = 4.5 \mu_B$, and $K = 1$ meV. In Fig. S7 we only consider positive values of H_z (as we did in the cartoon Fig. 2 in the main text) which reflect a ramping-down protocol. Thus, the relevant states to consider, other than the two degenerate AFM domains (Fig. S7, bottom left cartoons), are the “spin-flop ↑” states (bottom center), where the Néel vector is perpendicular to \hat{z} and the spins are canted toward $+\hat{z}$; and the BL ↑ states (bottom right) where top and bottom surface spins are pinned along $+\hat{z}$ and the ferromagnetically coupled bilayer has spins pointing up. We use the same labeling for the three possible BL states as in the main text; in particular, BL3 refers to the state where the bilayer is formed at the top surface which in our toy model is the

surface which has an exchange differing from the bulk J^{AFM} (bottom left cartoon).

First, in Fig. S7(a) we plot the energy of these different magnetic configurations per six-layer unit cell as a function of applied field H_z for a *bulk* unit cell, where the top and bottom spins in the unit cell have periodic boundary conditions along \hat{z} . As mentioned in the main text, with our stated parameters we get a spin-flop field $H_{\text{bulk}}^{\text{SF}} = 17$ T at the point where the collinear AFM states become lower energy than the SF ↑ state. Note that to calculate the energy of a concrete spin-flop ↑ phase we have canted the spins at an arbitrary 45° angle with respect to \hat{z} ; thus, the exact $H_{\text{bulk}}^{\text{SF}}$ in the model might shift up or down slightly depending on the actual lowest-energy angle of the spins in the spin-flop phase.

Most importantly however, with periodic boundary conditions and no surface spins, there is no range of fields where the BL states are lowest in energy.

In Fig. S7(b), we plot the energy given by Eq. S4 for the same six-layer unit cell, but this time we enforce vacuum boundary conditions such that the top and bottom spins in the unit cell each have only a single neighboring AFM-coupled layer. At this stage however, we assume the exchanges for top and bottom surface spins both remain equal to J^{AFM} , corresponding to the surface exchange asymmetry $x = 0$. Now, there is a region of fields between ~ 10 T – 22 T where the BL states, rather than the spin-flop or AFM states, are the lowest in energy. The field where the spin-flop \uparrow state becomes lower than the BL states gets moved to higher values compared to the bulk case, $H_{\text{slab}}^{\text{SF}} \sim 22$ T. However, because the surface exchanges are identical, all three possible BL states are degenerate in energy. As we argued intuitively and showed via committor evaluation in the main text, this degeneracy means that subsequent evolution to an AFM state as H_z is decreased to zero is not deterministic when $x = 0$.

In Figs. S7(c) and (d), we plot energy vs. H_z for vacuum-terminated slabs which have different AFM exchanges; in particular, as shown in the bottom left cartoon, we vary interlayer exchange at the top surface by a surface exchange asymmetry x such that $J^{\text{AFM}} \rightarrow (1+x)J^{\text{AFM}}$ (identically to the main text). We include results for both negative and positive values of x , specifically $x = -0.3$ and $x = +0.3$ in Figs. S7(c) and (d) respectively. Just like for the symmetric slab in Fig. S7 in Fig. S7(b), we get a finite window of fields where BL states are energetically preferred. Now however, the BL3 state becomes either lower (c) or higher (d) in energy than the other BL states BL1 and BL2. As we showed in this work, this breaking of degeneracy for intermediate multidomain BL states leads to an inequivalence in the probabilities to transition to the two AFM monodomain states. The domain which is preferentially selected for a given value of x will be opposite compared to the ramping-down case for the ramping-up direction, where the BL states will have spins pinned along $-\hat{z}$.

Finally, we note that in choosing the value of magnetic field H_z at which to evaluate physically meaningful committors to transition from any of the BL states to either AFM domain, it is necessary to choose a field magnitude at which are AFM states are lower-energy than the BL states, such that these transitions are probable. Thus, we chose +4T (–4T) for ramping-down (ramping-up) protocols, since from Fig. S7 and analogous figures we generated from $x = -0.5$ to $x = 0.5$, it is clear that at these fields the AFM states are always lower energy than the BL states for the range of surface exchange asymmetries we considered in the main text and in SI 3.

7. Simulations of MOKE using magnetization-field data from Monte Carlo

In Fig. 4(b) of the main text we show RCD (i.e. imaginary part of MOKE) signal calculated for magnetic configurations found by MC simulations. To calculate the complex MOKE signal we employ the transfer matrix approach, and use dielectric properties of MBT. Here we briefly recount the relevant methodological aspects, while more details can be found in Ref. [11].

Within this approach, each layer is considered as a material whose dielectric properties depend on the layer magnetization. Conceptually, the reflectivity matrix of such a slab is found by solving boundary conditions at each interface between layers. In practice, this is done computationally following the transfer matrix approach as described in Ref. [27]. As in Ref. [11], we take the dielectric tensor of MBT to be equal to

$$\varepsilon_C = \begin{pmatrix} \varepsilon_+ & 0 \\ 0 & \varepsilon_- \end{pmatrix} \quad (\text{S5})$$

in the basis of circular polarization. The diagonal elements of the k -th layer are given by the Lorentzian:

$$\varepsilon_{\pm}^k(\omega) = \varepsilon_{\infty} + \frac{f}{(\omega_0 \pm \delta\omega \frac{m_z^k}{m^s})^2 - \omega^2 - i\gamma\omega}, \quad (\text{S6})$$

where f , ω_0 , and γ are oscillator strength, resonant frequency, and damping. These parameters, together with a background contribution, ε_{∞} , are chosen to reproduce the measured optical conductivity in the spectral range of interest, reported in Ref. [28]. The difference in resonance frequency for LC and RC polarized light for a saturated layer magnetization, $\delta\omega$, is chosen to fit the magnitude of the RCD spectrum at the spin-flop transition. Saturation magnetization is taken to be $m^s = 4.5\mu_B$, as obtained by DFT for the magnetic ground state [11], while m_z^k is the average z component of the Mn moment in layer k . The effective splitting between the resonant frequency for the RC and LC light for layer k is then reduced from $\delta\omega$ by the ratio m_z^k/m^s . The MC simulation yields m_z^k for each layer; this is how we calculate MOKE for the MC structures. All the dielectric parameters are kept the same as in Ref. [11]; we reproduce them in Table S1 for convenience.

γ/ω_0	$f/(\omega_0^2\varepsilon)$	$\omega_0[\text{eV}]$	$\delta\omega[\text{eV}]$	$\varepsilon_{\infty}/\varepsilon$
0.424	4.2	2.05	-0.0708	$8.25 + 10.9i$

TABLE S1: Parameters of the Lorentz model (Eq. S6), used for MOKE simulations.

One more parameter needed for the MOKE calculation is the layer thickness. In Ref. [11] the experimental value of $d_{\text{exp}} = 1.3\text{nm}$ was used, and with realistic dielectric parameters (Tab. S1) we found that the reflectance becomes insensitive to the number of layers for slabs thicker

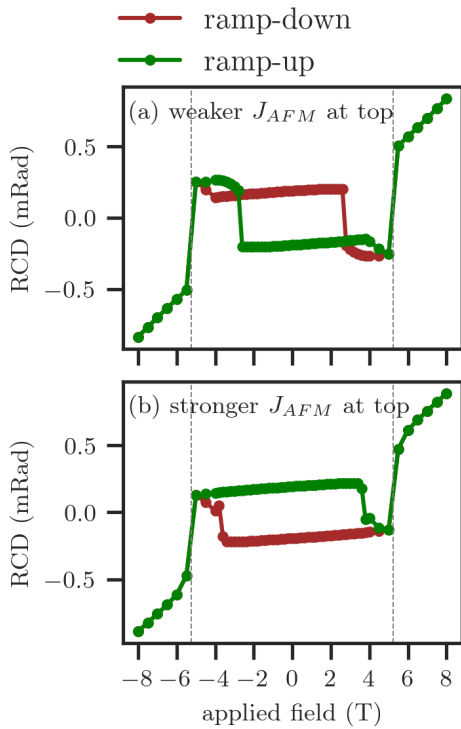


FIG. S8: Simulated RCD measurements at 2.3eV for the MC magnetic structures found for $x = -0.4$ in the 48 layer slab. We show the results for the surface with (a) the weaker exchange and (b) the stronger exchange at the top of the slab (exposed to light). The dashed lines denote the spin-flop transition field, $H_z^{SF} \approx 5.25$ T.

than ≈ 60 layers, or 80nm. The experimental slab thick-

ness of ≈ 130 nm is therefore firmly in the bulk limit, while even the 48 layer thick MC slab is not. To compensate for this difference, and enable the comparison to the experiment, we set $d = 2d_{exp}$ in the simulations - this ensures that the simulated MOKE is not sensitive to the bottom surface. Based on the understanding of MOKE in AFMs [11], we expect this quantitative change does not alter the qualitative picture.

We now have the tools to calculate MOKE for magnetic structures found by MC simulations, at any photon energy. First, we do this for the 48 layer slab with $x = -0.4$ and the photon energy of 2.3eV, comparable to the value used for experiments reported in Fig. 2 of Ref. [11]. In Figs. S8(a,b) we plot RCD for two configurations: for light shining on the surface with weaker and stronger exchange, respectively. In both cases the sign of RCD is trainable by the field protocol, and the spin-flop transition is found at $H_z^{SF} \approx 5.25$ T, marked by the dashed lines. Further, in both cases the RCD exhibits discontinuities at fields of smaller magnitude than H_z^{SF} , denoted H_z^* in the main text. The value of H_z^* , as well as the switching process itself, vary between the panels, reflecting different properties of probed surfaces.

We note that the simulation for more strongly coupled spins at the surface exposed to light (Fig. S8(b)) agrees better with the experimental data in Ref. [11]. This is consistent with the conclusion reached based on the spectroscopic study in Ref. [11], namely, that the surface spin exposed to light retains the orientation set by the field when the field is ramped towards $H_z = 0$. In contrast, as we discuss in the main text, in the transition to the AFM monodomain the spins on the surface with weaker exchange will flip opposite to the direction of the field as it is ramped towards $H_z = 0$.